UO_{2} Oxidative Corrosion by Nonclassical Diffusion

Joanne E. Stubbs, Anne M. Chaka, Eugene S. Ilton, Craig A. Biwer, Mark H. Engelhard, John R. Bargar, and Peter J. Eng

Phys. Rev. Lett. **114**, 246103 — Published 19 June 2015

DOI: 10.1103/PhysRevLett.114.246103

UO_2 Oxidative Corrosion by Non-classical Diffusion

Joanne E. Stubbs[1]*, Anne M. Chaka[2], Eugene S. Ilton[2], Craig A. Biwer[1]†, Mark H. Engelhard[3], John R. Bargar[4], and Peter J. Eng[1,5].

[1] *Center for Advanced Radiation Sources, University of Chicago, Chicago, IL, USA.*
[2] *Pacific Northwest National Laboratory, Richland, WA, USA.*
[3] *EMSL, Pacific Northwest National Laboratory, Richland, WA, USA.*
[4] *Stanford Synchrotron Radiation Lightsource, Menlo Park, CA, USA.*
[5] *James Franck Institute, University of Chicago, Chicago, IL, USA.*

Abstract
Using x-ray scattering, spectroscopy, and density-functional theory we determine the structure of the oxidation front when a UO_2 (111) surface is exposed to oxygen at ambient conditions. In contrast to classical diffusion and previously reported bulk UO_{2+x} structures, we find oxygen interstitials order into a nanoscale superlattice with three-layer periodicity and uranium in three oxidation states: IV, V, and VI. This oscillatory diffusion profile is driven by the nature of the electron transfer process, and has implications for understanding the initial stages of oxidative corrosion in materials at the atomistic level.

Main text
Oxidative corrosion is a key cause of material failure. This is especially true of uranium dioxide, which is the most economically important uranium mineral [1], the primary constituent of most nuclear fuels [2], and the desired product of many bioremediation strategies for uranium contamination [3]. UO_2 is an end-member in a complex metal-oxide system that is fundamentally important to experimental and computational actinide science [e.g., 4-7]. Despite more than 60 years of UO_2 oxidation research [8], moving beyond a macroscopic or empirical description to an understanding of the underlying atomistic processes has been difficult due to experimental challenges and the complex oxidation behavior of uranium oxides.

Uranium dioxide exhibits a broad range of structural transformations due to oxidation. The UO_2 lattice readily incorporates interstitial oxygen atoms up to a stoichiometry near $UO_{2.25}$ (U_4O_9) with minimal unit cell distortion [9]. Further oxidation to U_3O_8 leads to structural rearrangement, volume expansion, and material failure [10,11]. When U(IV) in UO_2 is oxidized to U(VI) under water, dissolution occurs since U(VI) readily forms soluble uranyl (UO_2^{2+}) that can be released into the environment, although surfaces can be passivated [12]. Single crystal surface structures and oxidation have been studied under vacuum [10,11,13-21], and by computational methods [22,23], but little is known about atomic level oxidation mechanisms under atmospheric conditions, especially in the earliest stages of oxidation.

We have combined crystal truncation rod (CTR) x-ray diffraction - an *in situ* method that is sensitive to surface atomic structure [24,25] - with density functional theory (DFT) and x-ray photoelectron spectroscopy (XPS) to detail the initial stages of UO_2 oxidation via the (111) surface, which is the natural cleavage plane and predicted to be the most stable when dry [26-28]. We show that the oxidation front does not follow classical diffusion, but instead exhibits

complex self-organization behavior, with interstitial oxygen atoms preferentially occupying every third layer below the surface.

A freshly polished surface was measured with CTR (time 0), exposed to ~1 atm dry oxygen gas, and re-measured several times up to 21 days (504 hours) of exposure [29]. As the surface oxidizes, broad, bulk-forbidden peaks develop at L values slightly greater than integers (Fig. 1; Ref [29], Fig. S1), consistent with a contracted three-slab (Ref [29], Fig. S2) superlattice in the surface-normal direction. Minor asymmetries (with shifts to higher L) about the Bragg peaks and valleys become more pronounced with increased O_2 exposure, indicating surface-normal contraction of the near-surface layers. The appearance of oscillations indicates development of a coherent thin layer with a different electron density extending a well-defined distance into the bulk. Oscillations appear on both off-specular and specular rods, demonstrating that the thin layer region shares the bulk in-plane order. These observations indicate an orderly advancing oxidation front that is distinct from classical exponential diffusion fronts.

Atomic-level models yielding excellent fits to the CTR data (Ref [29], Fig. S1) required inclusion of oxygen adatoms above the vacuum-terminated surface and refinement of the thicknesses and interstitial O atom occupancies for increasing numbers of structural slabs as oxidation proceeded. The refined slab contractions and interstitial oxygen occupancies are plotted vs. depth in Fig. 2. The extent of subsurface slab contractions and interstitial oxygen occupancies all increased with O_2 exposure. After 21 days of dry O_2 exposure, the oxidation front penetrated 11 slabs, or 35 Å into the crystal. Figure 2 reveals oscillatory profiles with three-layer periodicity in both slab contraction and interstitial O occupancy, with the longest exposures showing peaks in slab contraction in Slabs 0, 3, 6 and 9, and peaks in interstitial occupancy in Slabs 3 and 6. This three-slab periodicity is the source of the superlattice reflections and the increased electron density resulting from slab contraction and interstitial oxygen incorporation gives rise to the thickness oscillations. Additional CTR measurements (Ref [29], Fig. S3) of surfaces oxidized under more complex, aqueous conditions show a similar front develops, but at an accelerated rate, demonstrating that this oxidation mechanism applies over a broad range of conditions.

The source of the three-slab periodicity can be understood by considering the nature of uranium oxidation from a quantum mechanical perspective using partial densities of states (PDOS). Chaka et al. [23] used PDOS calculations to show that uranium oxidation can be quantified by the extent of electron transfer from localized U 5*f* bands to O 2*p* orbitals. Using a 1x1 seven-slab model with a fully oxygen-coordinated surface uranium, Chaka et al. found that interstitial oxygen occupation of either Slab 1, 2 or 3 resulted in the partial oxidation of three subsurface uranium atoms. Our present calculations on 1x1 systems (with an interstitial occupancy of either 0 or 1 in a given slab) show that if the surface uranium is oxidized by an oxygen adatom, it is thermodynamically most favorable to incorporate a layer of interstitial O into Slab 3 rather than Slab 1 or 2 due to greater availability of U 5*f* electrons. Deeper below the surface, the U 5*f* electron density is uniform and there is no thermodynamic driver for the initial interstitial oxygen atom to go below Slab 3 (Fig. 3a). Once Slab 3 is occupied, the availability of unoxidized U thermodynamically favors occupation of an additional interstitial layer in Slab 6 over Slabs 1, 2, 4 and 5 (Fig. 3a). The interstitial energy in Slab 7 is comparable to Slab 6; hence there is no thermodynamic driver to go deeper until Slab 6 is occupied.

Identifying the positions and quantifying the occupancies of oxygen interstitials in UO_2 is complicated by the large atomic number contrast between U (Z=92) and O (Z=8), but the CTR-derived occupancies are always << 1. DFT calculations are invaluable in interpreting the shifts in U atom positions that result from the interstitial oxygen atoms. The extent of measured Slab 3 contraction saturates at ~2.2% (Fig. 2a), and likely represents the maximum interstitial site occupation. DFT calculations of full, half and quarter slab occupancy for Slabs 3 and 6 result in Slab 3 contractions of 9.9%, 5.4%, and 2.4%, respectively, the latter consistent with the CTR measurements (Fig. 3b). Therefore, the maximum interstitial occupancy is likely about 25%. In this configuration, each interstitial O obtains a total of 0.71 electrons from its nearest, 0.84 electrons from its next-nearest, and 0.46 electrons from its next-next-nearest U neighbors (Ref [29], Fig. S4), creating a sphere of 38 oxidized U atoms around it that makes the occupation of adjacent interstitial sites less favorable. This charge delocalization results in subsurface U oxidation states distributed between IV and V while that of the topmost U is VI. Penetration of oxygen interstitials below the surface depends on availability of higher energy U 5*f* electrons at the Fermi level in multiple U atoms.

The CTR fit results [29] indicate that even under nominally anoxic conditions, the topmost U atoms are fully coordinated by O, OH^- or H_2O adatoms in positions that continue the bulk O lattice. The surface U atoms are relaxed into the bulk, broadly consistent with theoretical predictions of surface behavior under oxygen [22,23]. These findings differ from those of ultra-high vacuum (UHV) experiments, which indicate incomplete U coordination and outward relaxation of U atoms [15]. DFT calculations indicate that an O-terminated surface should have a $U\text{-}O_{adatom}$ bond length of ~1.8 Å regardless of whether subsurface interstitials are present, and the surface U should be fully oxidized to U(VI), producing a surface species that resembles half of the uranyl cation [22,23]. Our calculations indicate this "hemi-uranyl" termination energetically favors incorporation of the first oxygen interstitial layer into Slab 3, as observed with CTR, whereas hydroxyl termination slightly favors Slab 2 (Fig. 3a). XPS analysis of a surface oxidized for 20 days under O_2 gas showed the presence of U(IV), U(V) and U(VI) (Fig. 4), broadly consistent with the DFT results and previous spectroscopic measurements, e.g. [70,71]. Although U(VI) is the thermodynamically stable form of U under our measurement conditions, the oxidized U speciation is dominated by U(V) as a result of kinetic limitations to oxidation. We detected neither U(V) nor U(VI) on an unoxidized control sample. Given the presence of U(VI) on the oxidized sample and the first interstitial layer occupation of Slab 3, the surfaces are likely at least partially hemi-uranyl terminated. The CTR measurements show longer average adatom bond lengths (2.2-2.4 Å) than those predicted by DFT. Furthermore, the fraction of XPS signal arising from U(VI) is too small for the surface to be fully hemi-uranyl terminated [29]. The surface was prepared using deoxygenated aqueous solutions, and no effort was made to remove bound hydroxyl or water [29], which would require heating in UHV. Previous theoretical studies predict surface U-OH and $U\text{-}OH_2$ bond lengths of 2.2 and 2.6 Å, respectively [22,28], consistent with the CTR results. Given that the binding energy difference between Slab 2 and Slab 3 interstitials for a hydroxylated surface is very small (Fig. 3a), a mixed termination with some hemi-uranyl component could readily drive the first layer of interstitials into Slab 3. We therefore infer a mixed termination with hemi-uranyl, hydroxyl and/or molecular water at the surface.

The models determined from our CTR and DFT analyses are distinct from previously proposed bulk interstitial cluster models e.g. [5,7,9,11,30,34,40,45,47,48], few of which are periodic structures with long-range order. The superlattice peaks can only arise from a structure with 3-layer periodicity in the <111> direction. They cannot be explained by a surface layer of β-U_4O_9 with the structure determined by Cooper et al. [30]. Allen et al. [11] proposed that interstitial clusters might "plate out" between (111) planes in UO_{2+x}, however, their model is inconsistent with enhanced contraction of every third layer. The ordered, oscillatory oxidation front discovered here is driven by the surface and the energetics of the U 5*f* orbitals. Since corrosion is inherently surface mediated, it is ultimately the surface-imposed structure that is most relevant to low-temperature UO_2 corrosion. Using surface scattering and spectroscopy, combined with theory, we have demonstrated non-classical diffusion of oxygen interstitials into this redox-active material. Each interstitial has a sphere of influence extending over several shells of neighboring cations, influencing the positions and energetics of subsequent interstitials. This provides a conceptual framework to understand the initial stages of oxidation in UO_2, and may be relevant to a wide class of redox-active materials and minerals that can incorporate interstitial oxygen, including isostructural PuO_2.

*Correspondence to: stubbs@cars.uchicago.edu.
† Current Address: Department of Computational Medicine and Bioinformatics, University of Michigan, Ann Arbor, MI, USA

References

[1] R. Finch and T. Murakami, Reviews in Mineralogy **38**, 91 (1999).
[2] P. D. Wilson, *The nuclear fuel cycle: from ore to wastes* (Oxford University Press, New York, 1996).
[3] J. R. Bargar, R. Bernier-Latmani, D. E. Giammar, and B. M. Tebo, Elements **4**, 407 (2008).
[4] S. Conradson, D. Manara, F. Wastin, D. Clark, G. Lander, L. Morales, J. Rebizant, and V. Rondinella, Inorganic Chemistry **43**, 6922 (2004).
[5] G. C. Allen, P. A. Tempest, and J. W. Tyler, Nature **295**, 48 (1982).
[6] B. Willis, Nature **197**, 755 (1963).
[7] J. Wang, R. Ewing, and U. Becker, Scientific Reports **4**, ARTN 4216 (2014).
[8] F. Geønvold and H. Haraldsen, Nature **162**, 69 (1948).
[9] B. T. M. Willis, Journal of the Chemical Society-Faraday Transactions II **83**, 1073 (1987).
[10] G. C. Allen, P. A. Tempest, and J. W. Tyler, Philosophical Magazine B-Physics of Condensed Matter Statistical Mechanics Electronic Optical and Magnetic Properties **54**, L67 (1986).
[11] G. C. Allen, P. A. Tempest, and J. W. Tyler, Journal of the Chemical Society-Faraday Transactions I **84**, 4061 (1988).
[12] D. W. Shoesmith, Journal of Nuclear Materials **282**, 1 (2000).
[13] W. P. Ellis, Journal of Chemical Physics **48**, 5695 (1968).

[14] W. Ellis and T. Taylor, Surface Science **91**, 409 (1980).
[15] K. Thompson, W. Ellis, W. Taylor, S. Valone, and C. Maggiore, Nuclear Instruments & Methods in Physics Research **218**, 475 (1983).
[16] M. R. Castell, C. Muggelberg, G. A. D. Briggs, and D. T. Goddard, Journal of Vacuum Science & Technology B **14**, 966 (1996).
[17] M. R. Castell, C. Muggelberg, S. L. Dudarev, A. P. Sutton, G. A. D. Briggs, and D. T. Goddard, Applied Physics A - Materials Science & Processing **66**, S963 (1998).
[18] G. C. Allen, P. A. Tempest, and J. W. Tyler, Journal of the Chemical Society-Faraday Transactions I **84**, 4049 (1988).
[19] W. P. Ellis, in *Fundamentals of Gas-Surface Interactions*, edited by H. Salstburg, J. Smith, J.N., and M. Rogers (Academic Press, New York, 1967), pp. 89.
[20] R. Wang, Spent Fuel Special Studies Progress Report: Probable Mechanisms for Oxidation and Dissolution of Single Crystal UO_2 Surfaces, 1981.
[21] C. Muggelberg, M. R. Castell, G. A. D. Briggs, and D. T. Goddard, Surface Review and Letters **5**, 315 (1998).
[22] F. N. Skomurski, L. C. Shuller, R. C. Ewing, and U. Becker, Journal of Nuclear Materials **375**, 290 (2008).
[23] A. Chaka, G. Oxford, J. Stubbs, P. Eng, and J. Bargar, Computational and Theoretical Chemistry **987**, 90 (2012).
[24] P. Fenter, Applications of Synchrotron Radiation in Low-Temperature Geochemistry and Environmental Sciences **49**, 149 (2002).
[25] I. Robinson, Physical Review B **33**, 3830 (1986).
[26] A. Tan, R. Grimes, and S. Owens, Journal of Nuclear Materials **344**, 13 (2005).
[27] F. N. Skomurski, R. C. Ewing, A. L. Rohl, J. D. Gale, and U. Becker, American Mineralogist **91**, 1761 (2006).
[28] Z. Rak, R. Ewing, and U. Becker, Surface Science **608**, 180 (2013).
[29] See Supplemental material at (web address), which includes Refs. [30-69], for experimental and computational methods, details about the UO_2 structure, and additional figures.
[30] R. I. Cooper and B. T. M. Willis, Acta Crystallographica Section A **60**, 322 (2004).
[31] D. J. M. Bevan, I. E. Grey, and B. T. M. Willis, Journal of Solid State Chemistry **61**, 1 (1986).
[32] B. Belbeoch, J. C. Boiveneau, and P. Perio, Journal of Physics and Chemistry of Solids **28**, 1267 (1967).
[33] F. Garrido, A. C. Hannon, R. M. Ibberson, L. Nowicki, and B. T. M. Willis, Inorganic Chemistry **45**, 8408 (2006).
[34] A. D. Murray and B. T. M. Willis, Journal of Solid State Chemistry **84**, 52 (1990).
[35] N. C. Popa and B. T. M. Willis, Acta Crystallographica Section A **60**, 318 (2004).
[36] B. T. M. Willis, Proceedings of the Royal Society of London, Series A (Mathematical and Physical Sciences) **274**, 122 (1963).
[37] B. T. M. Willis, Journal de Physique **25** (1964).
[38] D. A. Andersson, J. Lezama, B. P. Uberuaga, C. Deo, and S. D. Conradson, Physical Review B **79** (2009).
[39] S. Conradson *et al.*, Journal of Solid State Chemistry **178**, 521 (2005).
[40] G. C. Allen and P. A. Tempest, Journal of the Chemical Society-Dalton Transactions, 2169 (1982).

[41] G. C. Allen, J. T. Buswell, and P. A. Tempest, Journal of the Chemical Society-Dalton Transactions, 589 (1983).
[42] G. C. Allen and P. A. Tempest, Journal of the Chemical Society-Dalton Transactions, 2673 (1983).
[43] G. C. Allen and P. A. Tempest, Proceedings of the Royal Society of London Series a-Mathematical Physical and Engineering Sciences **406**, 325 (1986).
[44] B. T. M. Willis, Acta Crystallographica Section A **34**, 88 (1978).
[45] F. Skomurski, J. Wang, R. Ewing, and U. Becker, Journal of Nuclear Materials **434**, 422 (2013).
[46] G. C. Allen, P. A. Tempest, and J. W. Tyler, Journal of the Chemical Society-Faraday Transactions I **83**, 925 (1987).
[47] H. Geng, Y. Chen, Y. Kaneta, and M. Kinoshita, Applied Physics Letters **93**, ARTN 201903 (2008).
[48] H. Geng, Y. Chen, Y. Kaneta, and M. Kinoshita, Physical Review B **77**, ARTN 180101 (2008).
[49] K. B. Alberman and J. S. Anderson, Journal of the Chemical Society (Resumed) **1949**, S303 (1949).
[50] M. Schmidt, P. Eng, J. Stubbs, P. Fenter, and L. Soderholm, Review of Scientific Instruments **82**, ARTN 075105 (2011).
[51] Python Data Shell, https://github.com/xraypy/tdl, 2014.
[52] M. Bjorck and G. Andersson, Journal of Applied Crystallography **40**, 1174 (2007).
[53] M. Bjorck, Journal of Applied Crystallography **44**, 1198 (2011).
[54] GenX, http://genx.sourceforge.net, 2014.
[55] E. S. Ilton, J. S. L. Pacheco, J. R. Bargar, Z. Shi, J. Liu, L. Kovarik, M. H. Engelhard, and A. R. Felmy, Environmental Science & Technology **46**, 9428 (2012).
[56] E. J. Schofield *et al.*, Environmental Science & Technology **42**, 7898 (2008).
[57] J. H. Liu, S. Van den Berghe, and M. J. Konstantinovic, Journal of Solid State Chemistry **182**, 1105 (2009).
[58] N. Belai, M. Frisch, E. S. Ilton, B. Ravel, and C. L. Cahill, Inorganic Chemistry **47**, 10135 (2008).
[59] E. S. Ilton and P. S. Bagus, Surface and Interface Analysis **43**, 1549 (2011).
[60] M. Seah and R. White, Surface and Interface Analysis **33**, 960 (2002).
[61] C. Powell, A. Jablonski, W. Werner, and W. Smekal, Applied Surface Science **239**, 470 (2005).
[62] S. Tanuma, C. Powell, and D. Penn, Surface and Interface Analysis **21**, 165 (1994).
[63] J. Castle and M. Baker, Journal of Electron Spectroscopy and Related Phenomena **105**, 245 (1999).
[64] D. Briggs and M. P. Seah, *Practical Surface Analysis* (John Wiley & Sons Ltd., 1990), Vol. 1: Auger and X-ray Photoelectron Spectroscopy.
[65] J. Perdew, K. Burke, and M. Ernzerhof, Physical Review Letters **77**, 3865 (1996).
[66] K. Kudin, G. Scuseria, and R. Martin, Physical Review Letters **89**, ARTN 266402 (2002).
[67] B. Delley, J Chem Phys **92**, 508 (1990).
[68] B. Delley, Computational Materials Science **17**, 122 (2000).
[69] B. Delley, Journal of Chemical Physics **113**, 7756, PII [S0021-9606(00)30342-7] (2000).

[70] B. G. Santos, H. W. Nesbitt, J. J. Noel, and D. W. Shoesmith, Electrochimica Acta **49**, 1863 (2004).
[71] K. O. Kvashnina, S. M. Butorin, P. Martin, and P. Glatzel, Physical Review Letters **111**, 253002 (2013).

Acknowledgements

CTR data were collected at GeoSoilEnviroCARS, using resources of the Advanced Photon Source, a U.S. DOE Office of Science User Facility operated for the DOE Office of Science by Argonne National Laboratory (DE-AC02-06CH11357). GeoSoilEnviroCARS is supported by NSF - Earth Sciences (EAR-1128799) and DOE-BES - GeoSciences (DE-FG02-94ER14466). Chaka and Ilton were supported by the Geosciences Research Program at PNNL, US DOE Office of Science, Office of Basic Energy Sciences, Division of Chemical Sciences, Geosciences & Biosciences. Support was provided by DOE-BER, Subsurface Biogeochemical Research, through the SLAC SFA program (DOE contract DE-AC02-76SF00515). XPS data were collected in the Radiochemistry Annex at EMSL, and a portion of the DFT study was performed using the computational resources of EMSL, a national scientific user facility sponsored by DOE-BER and located at Pacific Northwest National Laboratory. Early sample preparation benefitted from access to the Berkeley Nanogeoscience Center. We thank R. Caciuffo (Institute for Transuranium Elements) and M. Paffett (Los Alamos National Laboratory) for providing UO_2 crystals.

Fig. 1

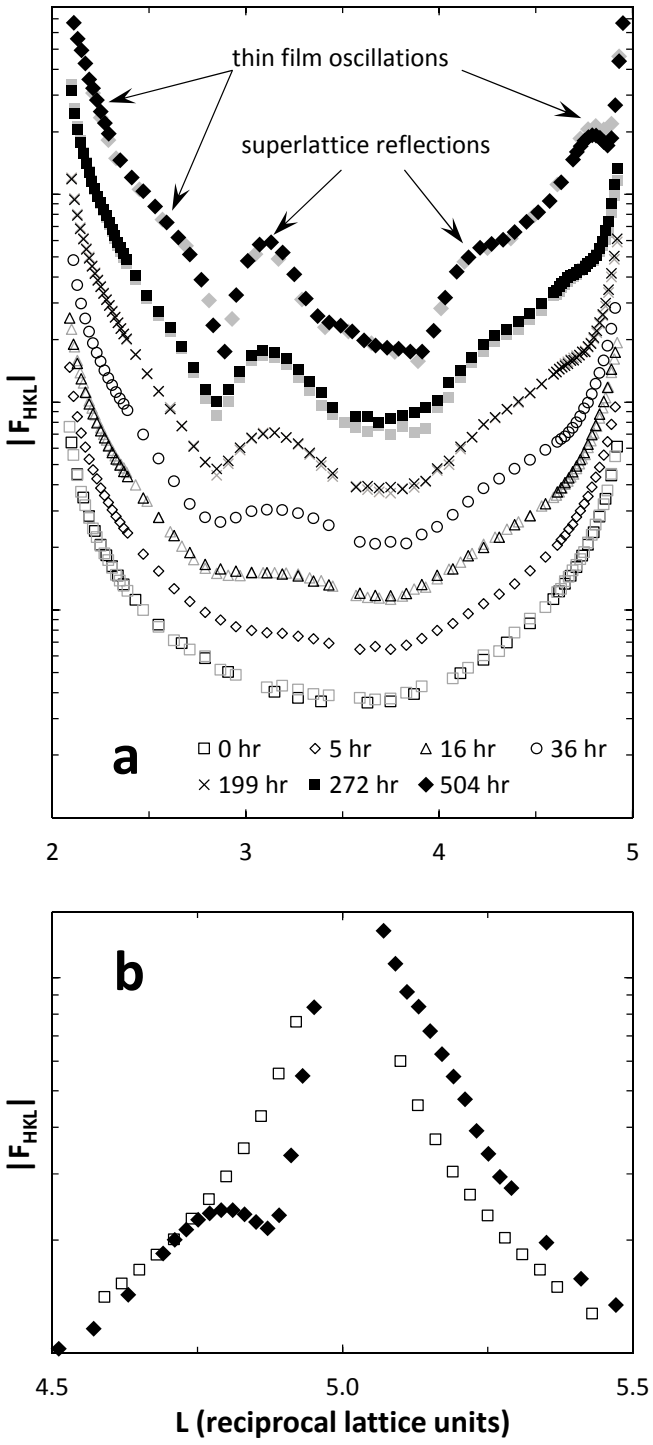
thin film oscillations
superlattice reflections
|F_HKL|
a
0 hr
5 hr
16 hr
36 hr
199 hr
272 hr
504 hr
2
3
4
5
b
|F_HKL|
4.5
5.0
5.5
L (reciprocal lattice units)

Fig. 2

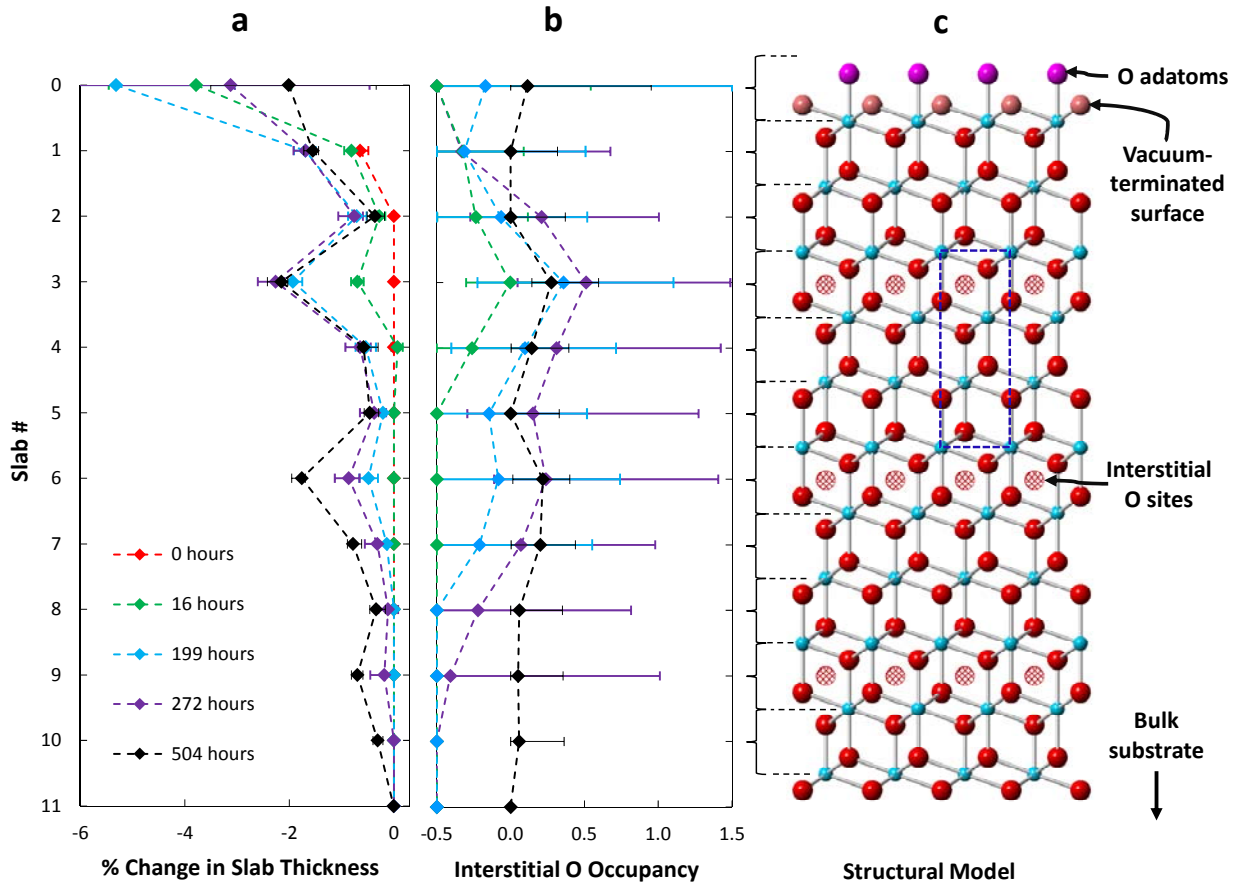
a
b
c
Slab #
0
1
2
3
4
5
6
7
8
9
10
11
-6
-4
-2
0
-0.5
0.0
0.5
1.0
1.5
0 hours
16 hours
199 hours
272 hours
504 hours
% Change in Slab Thickness
Interstitial O Occupancy
Structural Model
O adatoms
Vacuum-terminated surface
Interstitial O sites
Bulk substrate

Fig. 3

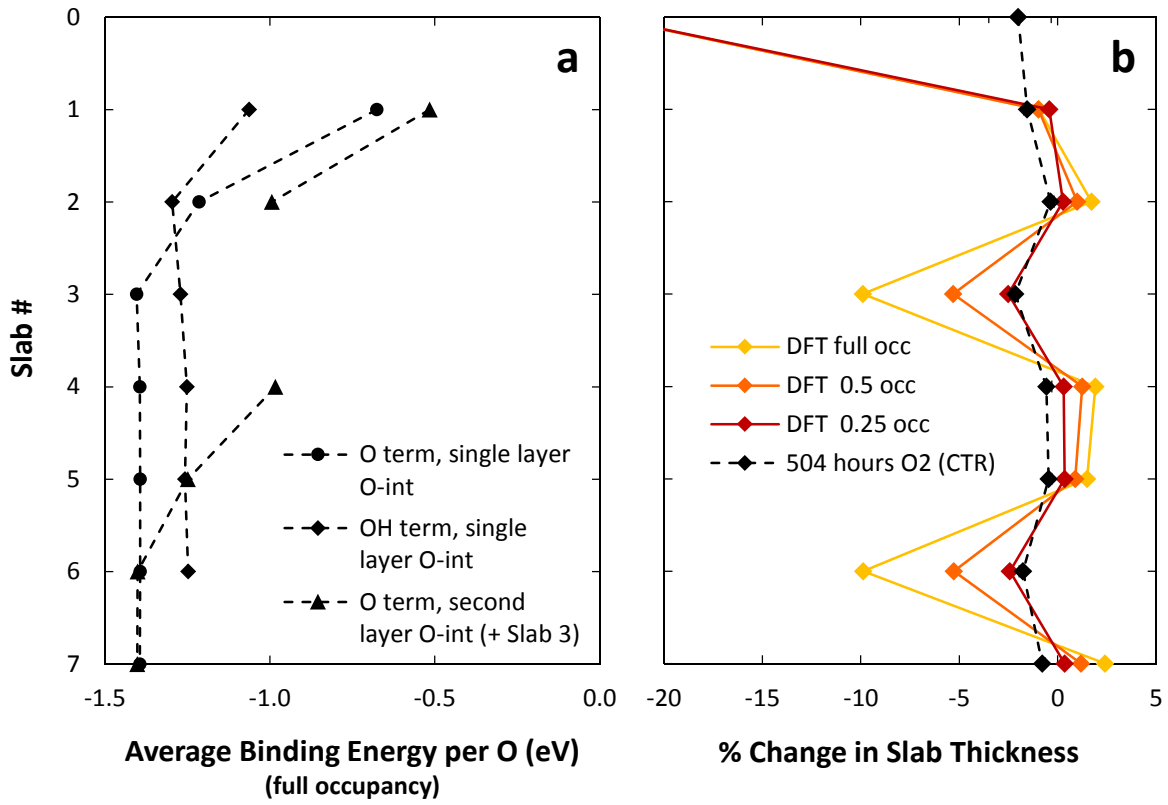
a
b
Slab #
0
1
2
3
4
5
6
7
-1.5
-1.0
-0.5
0.0
-20
-15
-10
-5
0
5
O term, single layer O-int
OH term, single layer O-int
O term, second layer O-int (+ Slab 3)
DFT full occ
DFT 0.5 occ
DFT 0.25 occ
504 hours O2 (CTR)
Average Binding Energy per O (eV)
(full occupancy)
% Change in Slab Thickness

Fig. 4

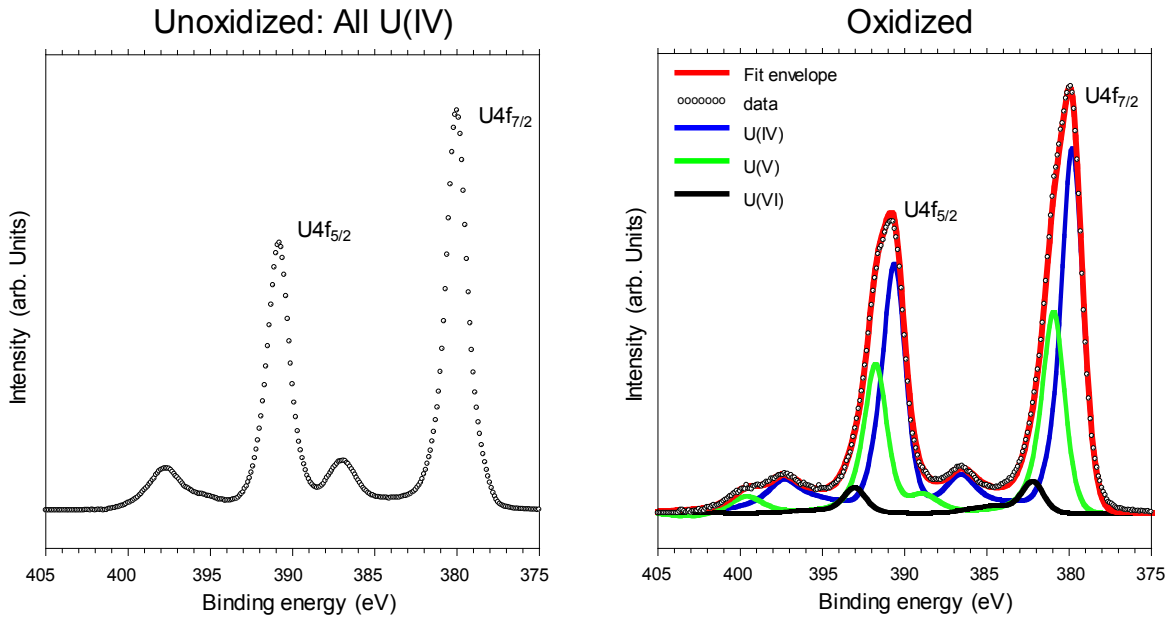
Unoxidized: All U(IV)
Intensity (arb. Units)
U4f5/2
U4f7/2
405
400
395
390
385
380
375
Binding energy (eV)
Oxidized
Fit envelope
data
U(IV)
U(V)
U(VI)
U4f5/2
U4f7/2
Intensity (arb. Units)
405
400
395
390
385
380
375
Binding energy (eV)

Figure Captions

Fig. 1. 10L rod segments collected during oxidation. (a) Oxidation is accompanied by development of superlattice reflections and thin-film oscillations. Statistical error bars are smaller than symbols. Data collected at the start (black symbols) and end (gray symbols) of long data sets show surfaces were stable during measurement. (b) Region around 105 Bragg peak shows development of asymmetry and oscillations upon oxidation.

Fig. 2. (color online) Refined slab contractions (a) and interstitial occupancies (b) are plotted vs. depth and show 3-layer periodicity. (c) Proposed model for oxidized UO_2 (111) surface. Cyan = U, Red = structural O, Magenta = surface O adatoms, Hatched Red = interstitial O. Surface is oxygen terminated. Y-Z projection of surface unit cell is indicated by blue dashed lines.

Fig. 3. (color online) DFT results (a) Binding energies for one layer of interstitial oxygen atoms below hemi-uranyl (oxygen) and hydroxyl-terminated 1x1 surfaces, and for a second layer below the hemi-uranyl terminated 1x1 surface when the Slab 3 interstitial position is occupied. (b) Predicted slab thickness changes for fully-, half- and quarter-occupied interstitial positions in Slabs 3 and 6 overlain on thickness changes derived from 504-hour CTR data.

Fig. 4. (color online) X-ray photoelectron spectra collected at normal emission. The nominally unoxidized surface shows strictly U(IV), whereas the oxidized surface shows significant U(V) and minor U(VI).